nature synthesis

Article

https://doi.org/10.1038/s44160-024-00562-0

Epitaxial growth of quantum dots on van der Waals surfaces

Received: 9 June 2023

Accepted: 9 May 2024

Published online: 04 June 2024

Check for updates

Kaiyao Xin[1,2,3,6], Lian Li[1,6], Ziqi Zhou[4,6], Chen Zhang[2,3], Juehan Yang[2,3], Hui-Xiong Deng[2,3], Jinchuan Zhang[1], Junqi Liu[1], Kaihui Liu[4], Can Liu[5] ✉, Fengqi Liu[1] ✉, Zhongming Wei[2,3] ✉ & Shenqiang Zhai[1] ✉

Zero-dimensional quantum dots (QDs), which have inherent quantum confinement effects and sharp discrete energy levels, are regarded as essential building blocks for quantum information devices. Current manufacturing strategies often exhibit limited adaptability in terms of compositional design or interface engineering. Here we propose a van der Waals (vdW) epitaxial strategy for growing intrinsic QDs by modulating the interfacial couplings between vdW surfaces and QDs. Versatile III–V (MX, M = Ga, In; X = As, Sb) and IV–VI (SnTe) QDs were fabricated without considering the lattice mismatch constraints, leading to QDs with more intrinsic features. We further demonstrated that the as-grown InSb QDs/MoS_2 showed a broadened photoresponse in the near-infrared region due to the efficient charge-transfer channels at their vdW interfaces. This work reports a synthetic route to the all-in-solid epitaxy of QDs, which may expand the optoelectronic applications of QDs beyond those that are conventionally grown.

Quantum dots (QDs), which have discrete energy levels, tunable electronic structures and robust photon–electron interactions, have attracted considerable attention in diverse fields, such as nonlinear optics[1,2], semiconductor lasers[3–5], photodetection[6–8] and quantum computing[9,10]. The efficacy of QDs in these application scenarios depends on their composition, morphology and interface features. Specifically, the composition of QDs dictates the functionalities available for specific applications, while the morphology modulates the electronic structures and energy levels. Furthermore, the interface between QDs and their substrates plays a crucial role in electron–phonon interactions and charge-transport processes. Therefore, the synthesis of QDs with customizable compositions, controllable morphologies and intrinsic interface properties is essential for fulfilling the diverse requirements of various applications.

To date, intensive efforts have been devoted to the preparation of QDs to satisfy the aforementioned needs. In particular, the colloidal solution process has emerged as a successful approach for fabricating QDs with highly controllable morphologies[11,12]. However, this method is limited to the use of IV–VI components (such as PbS (ref. 5), PbSe (ref. 13) and PdTe (ref. 14)) and transition-metal dichalcogenides (TMDs, such as ZnS (ref. 15), CdSe (ref. 16) and HgTe (ref. 17)) due to the scarcity of soluble precursors for alternative components. Moreover, the solution process inevitably introduces external contaminants, leading to extrinsic interfaces of QDs and substrates. In contrast, Stranski–Krastanov (SK) mode self-assembly epitaxy has demonstrated efficacy in producing high-quality III–V QDs, such as InAs[18,19] and InGaAs[20,21], with ultraclean interfaces. However, this method imposes stringent lattice mismatch constraints on substrates (typically a 5–10% mismatch degree), making component design exceedingly challenging and limiting its applicability to QD species beyond the III–V compounds. Additionally, stress release through lattice relaxation in SK mode epitaxy results in variations in shape and size of QDs, compromising the uniformity of QD-based devices. Therefore, there is a pressing need for a universal

[1]Laboratory of Solid-State Optoelectronics Information Technology, Institute of Semiconductors, Chinese Academy of Sciences, Beijing, China. [2]State Key Laboratory of Superlattices and Microstructures, Institute of Semiconductors, Chinese Academy of Sciences, Beijing, China. [3]Center of Materials Science and Optoelectronics Engineering, University of Chinese Academy of Sciences, Beijing, China. [4]State Key Laboratory for Mesoscopic Physics, Frontiers Science Center for Nano-optoelectronics, School of Physics, Peking University, Beijing, China. [5]Key Laboratory of Quantum State Construction and Manipulation (Ministry of Education), Department of Physics, Renmin University of China, Beijing, China. [6]These authors contributed equally: Kaiyao Xin, Lian Li, Ziqi Zhou. ✉e-mail: canliu@ruc.edu.cn; fqliu@red.semi.ac.cn; zmwei@semi.ac.cn; zsqlzsmbj@semi.ac.cn

https://doi.org/10.1038/s44160-024-00562-0

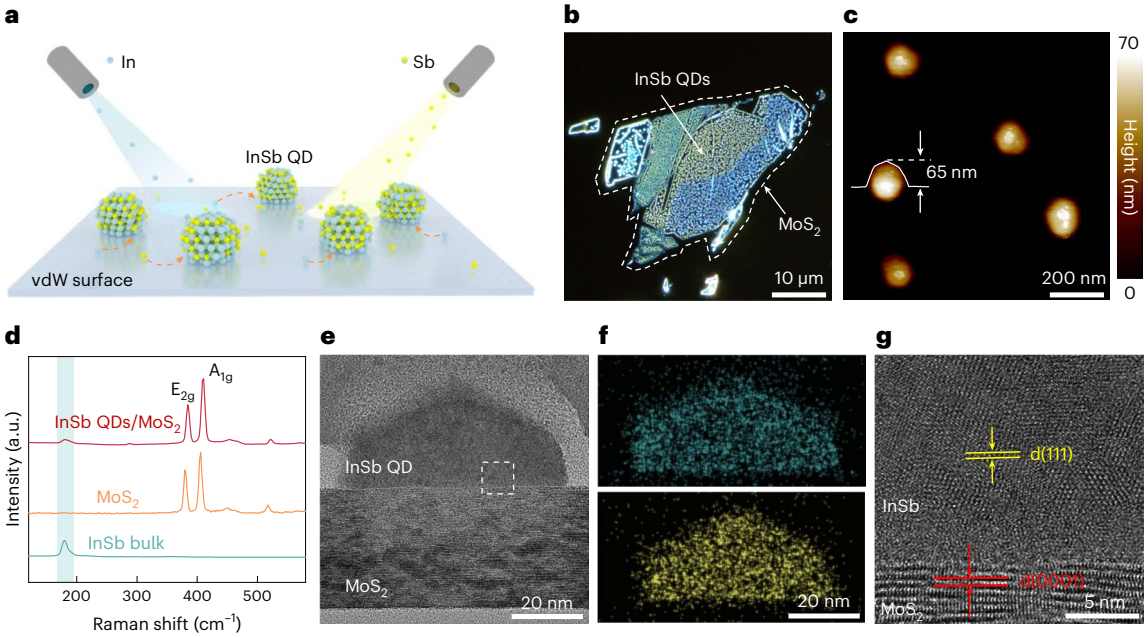

Fig. 1 | vdW epitaxy of InSb QDs on MoS_2. **a**, VdW epitaxy schematics: indium and antimony atoms were dispensed from heated cells to a MoS_2 surface without dangling bonds and then adsorbed and reacted to form InSb seeds, which ultimately grew into dispersed QDs. **b**, Dark-field optical image of InSb QDs on MoS_2, where black represents flatness and the colours indicate bulges. **c**, Atomic force microscopy image of InSb QDs on MoS_2, showing a large aspect ratio of ~0.5 (65 nm/130 nm). **d**, Raman spectra of InSb QDs/MoS_2, MoS_2 alone and the InSb bulk crystal. **e**, Cross-sectional TEM image of an InSb QD on MoS_2. **f**, EDS mapping of the InSb QD, demonstrating the uniform distribution of indium (the upper panel) and antimony (the lower panel). **g**, A magnified view of the interface between the InSb QD and MoS_2 indicated by the white square in **e**, revealing the parallel relationship between the InSb (111) facet and the MoS_2 (0001) facet.

method that balances component flexibility and morphology design while ensuring the presence of intrinsic interfaces in QDs.

In this work, we propose a universal strategy for fabricating QDs with customizable compositions, controlled morphologies and intrinsic interfaces by employing van der Waals (vdW) surfaces as epitaxy substrates. This method offers notable advantages: (1) the vdW interactions between two-dimensional (2D) layered materials and QDs overcome the limitations imposed by lattice mismatch, effectively expanding the diversity of QD compositions; (2) the optimal morphology of QDs with a large aspect ratio is easily achieved due to the low surface energy of the 2D vdW materials; and (3) an intrinsic interface between the QDs and the vdW substrate is ensured within the ultrahigh-vacuum molecular beam epitaxy (MBE) system, promoting effective interfacial coupling and supporting additional charge transfer. Therefore, the universal synthesis of QDs (including the III–V semiconductors InAs, InSb, GaAs and GaSb and the IV–VI semiconductor SnTe) with ideal morphologies and intrinsic interfaces with respect to the substrate was successfully realized on vdW surfaces, demonstrating synergistic advancements in photodetection with a broadened response range based on these mixed-dimensional heterostructures.

Epitaxial growth of InSb QDs on MoS_2 surfaces

In our design, we utilized MoS_2, a prototypical 2D vdW crystal that was mechanically exfoliated and transferred onto a SiO_2/Si substrate, to serve as a pristine vdW surface for QD epitaxy (see Methods for details). Indium and antimony atoms were separately evaporated from heated cells to facilitate the growth of the typical III–V compound InSb in the MBE system. Upon arriving at the substrate, the incident atoms were physically adsorbed and rapidly diffused on the vdW surface of MoS_2, and nucleation occurred when indium and antimony atoms effectively collided (Fig. 1a). After 1 min of growth, uniformly distributed InSb QDs with hemispherical shapes (with a typical diameter of ~130 nm) were successfully obtained on the MoS_2 surfaces (Fig. 1b,c). In addition, the size and density of the InSb QDs were apparently dependent on the thickness of MoS_2 (Extended Data Table 1), which was attributed to differences in the migration barrier of incident atoms (Supplementary Fig. 1). The presence of InSb QDs on MoS_2 was verified through Raman spectroscopy, which showed a characteristic InSb vibrational mode at ~180 cm^{-1} (Fig. 1d). A slight redshift of the Raman peak of the as-grown InSb QDs compared with that of the InSb bulk was observed, which was attributed to the synergetic effect of their stress-free nature and size reduction[22,23]. After transection with a focused ion beam, a hemispherical InSb QD with a large aspect ratio of ~0.5 and uniform elemental distribution was confirmed by transmission electron microscopy (TEM) and energy-dispersive X-ray spectroscopy (EDS) mapping, respectively (Fig. 1e,f). A magnified atomic-resolution TEM image of the interface between the InSb QD and MoS_2 clearly demonstrated their lattice configuration. As shown in Fig. 1g, the characteristic interplanar crystal distance of ~0.3 Å confirmed that the close-packed (111) facet of the InSb QDs was connected to the (0001) facet of MoS_2. Notably, the randomly distributed point defects on MoS_2 effectively facilitated QD nucleation with vdW contacts between them (Supplementary Fig. 2).

Mechanism of InSb QD epitaxy on MoS_2 vdW surfaces

To elucidate the mechanism of the epitaxial growth of QDs on vdW surfaces, we conducted first-principles calculations to investigate the growth kinetics and thermodynamic processes of non-layered InSb on the MoS_2 surface. As shown in Fig. 2a, physically adsorbed indium and antimony atoms diffused freely on the MoS_2 surface due to the absence of dangling bonds. Some effective collisions resulted in chemical bonds between atoms, leading to the formation of primitive InSb seeds (Extended Data Fig. 1). Furthermore, the ability to capture precursor atoms dominated the expansion of seeds in the out-of-plane direction. By analysing the diffusion of indium and antimony atoms on the MoS_2 surface and the nucleated InSb surface, respectively (Supplementary Fig. 3), it was concluded that precursor atoms migrated more easily on MoS_2 than on InSb due to the substantial difference in strength between vdW interactions and covalent bonds (Fig. 2b,c). Consequently, it was kinetically favourable for both incident and diffuse

https://doi.org/10.1038/s44160-024-00562-0

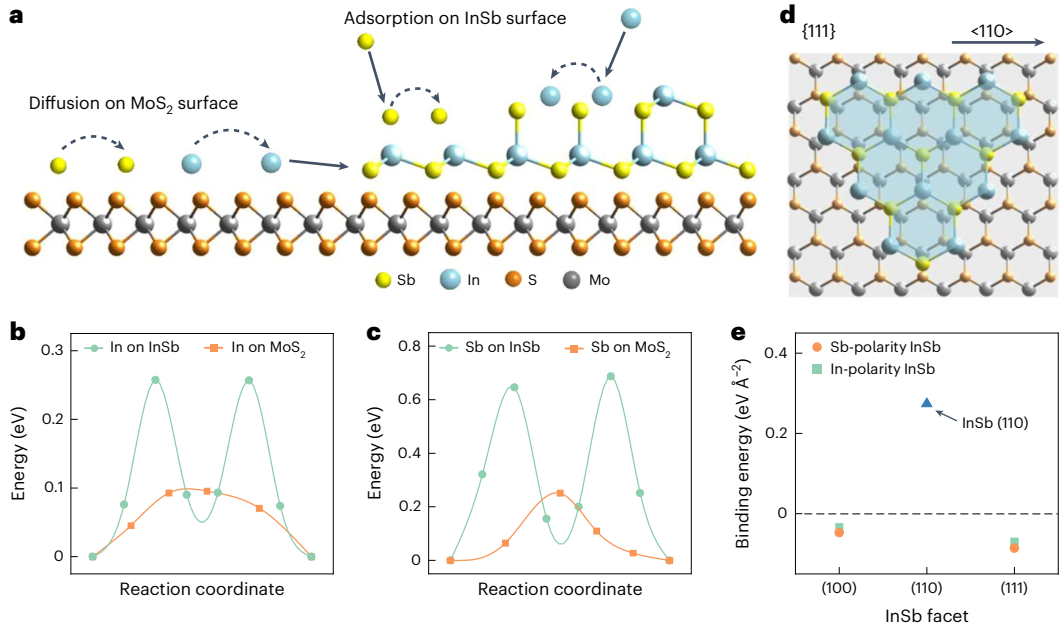

Fig. 2 | Theoretical simulation of the vdW epitaxial mechanism in the growth of InSb QDs on MoS_2. **a**, Schematic of the incident indium and antimony atoms freely diffusing on MoS_2 or easily captured by InSb seeds, demonstrating the kinetic processes involved in vdW epitaxy. **b**, Diffusion barriers of indium atoms on InSb and MoS_2 with the relative reaction coordinate along the abscissa. **c**, Diffusion barriers of antimony atoms on InSb and MoS_2 with the relative reaction coordinate along the abscissa. **d**, The energy-favoured configuration of InSb contacting MoS_2 where the interfaces shared the same C_{3v} symmetry. **e**, Quantitative theoretical analysis of the binding energy, indicating the most stable state of the InSb (111) facet on the MoS_2 (0001) facet.

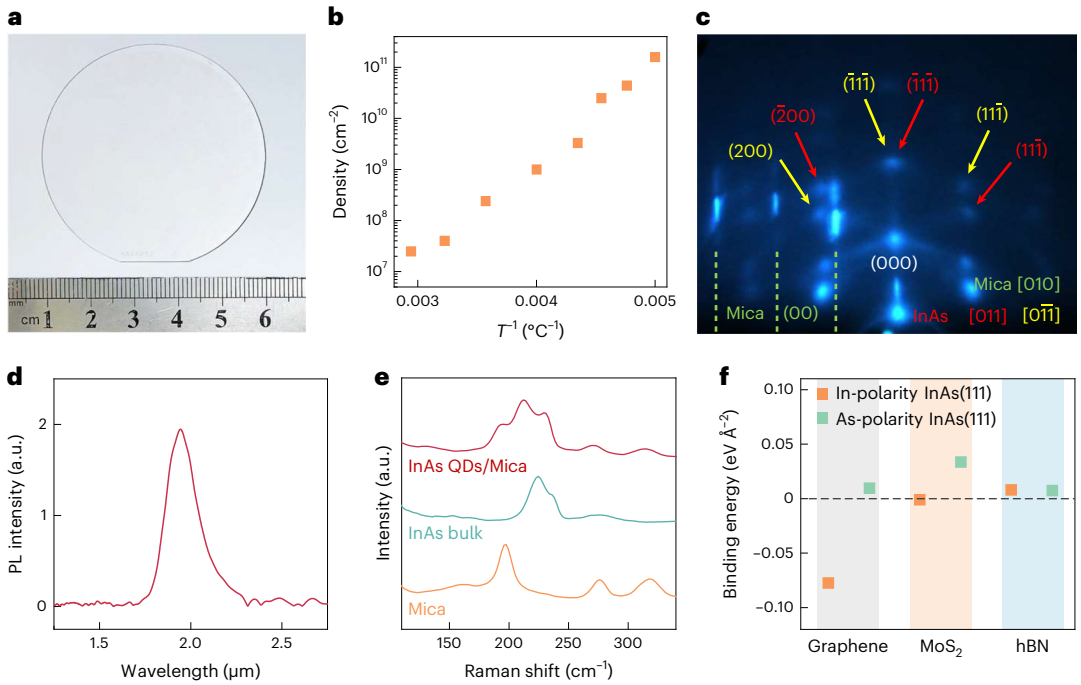

Fig. 3 | VdW epitaxy of uniformly distributed InAs QDs on wafer-scale FL mica. **a**, Photograph of a 2 inch FL mica wafer on which InAs QDs were grown. **b**, The temperature dependence of the density of InAs QDs on the FL mica surface. **c**, The electron diffraction pattern of InAs QDs on FL mica obtained by reflection high-energy electron diffraction, where the lines refer to FL mica and the spots represent InAs QDs along the [011] and [0$\bar{1}\bar{1}$] directions. **d**, PL spectrum of InAs QDs with a characteristic peak at ~1.93 μm measured at 77 K. **e**, Raman spectra of InAs QDs/FL mica, individual FL mica and bulk InAs crystal. **f**, Quantitative theoretical analysis of the binding energy for InAs (111) facet contacting the vdW surfaces of graphene, MoS_2 and hBN.

atoms to be readily captured by InSb seeds and not easily released due to their strong covalent bonds, promoting the growth of primitive InSb seeds. Moreover, high-surface-energy InSb tended to form a hemispherical morphology, thereby reducing the total surface energy on the MoS_2 (0001) facet, which is widely acknowledged to be driven by the lowest-energy principle. This combined modulation of thermodynamics and kinetics ensured the stable epitaxy of intrinsic hemispherical InSb QDs on the MoS_2 vdW surface. Additionally, the epitaxial relationship of QDs on MoS_2 surfaces could be thermodynamically modulated, even though there were only weak vdW interactions

https://doi.org/10.1038/s44160-024-00562-0

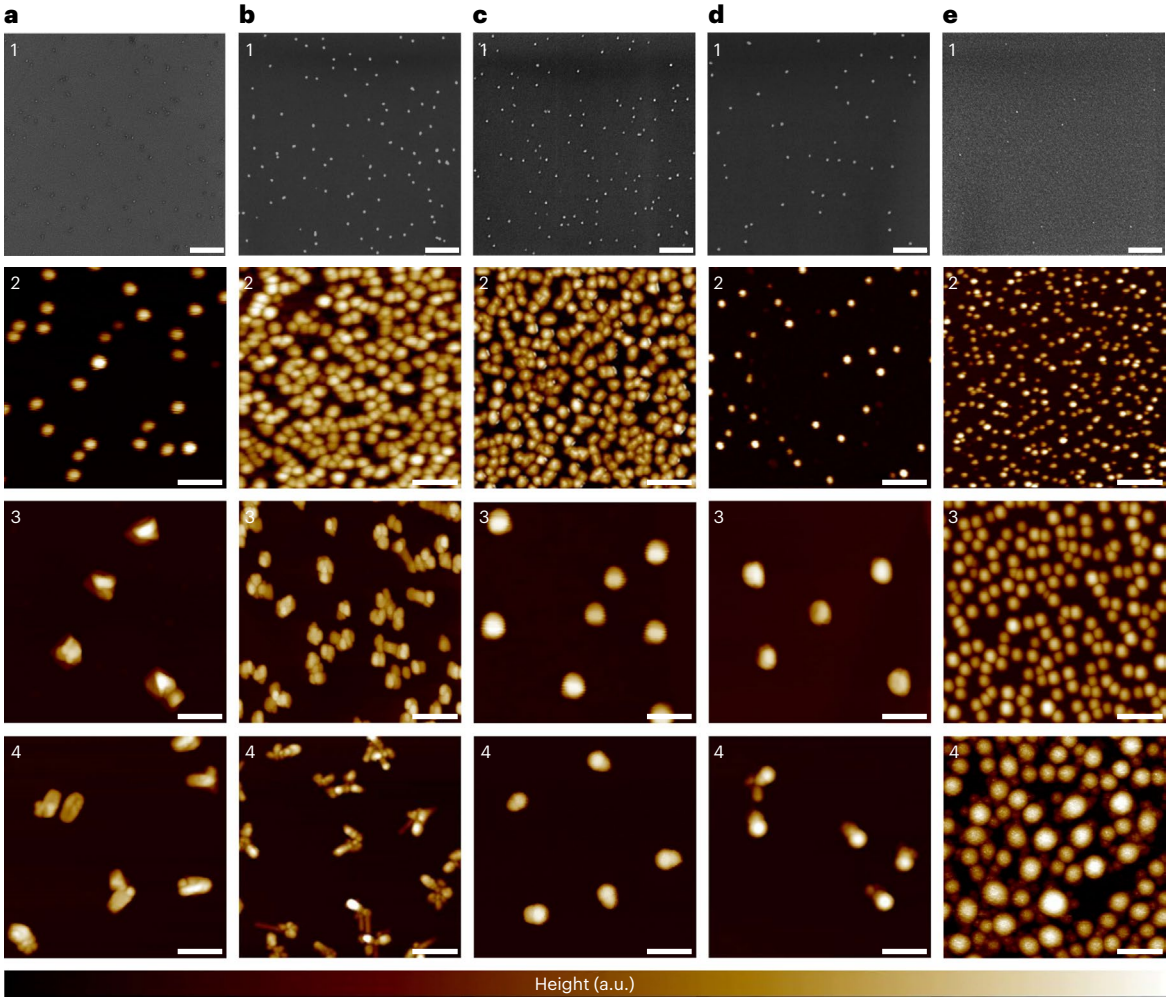

Fig. 4 | Universal fabrication of III–V and IV–VI QDs on vdW surfaces. **a**–**e**, InAs QDs (**a**), GaAs QDs (**b**), InSb QDs (**c**), GaSb QDs (**d**) and SnTe QDs (**e**) grown on (1) hBN, (2) FL mica, (3) MoS_2 and (4) graphene. With increasing interface coupling strength (hBN ≈ FL mica > MoS_2 > graphene), the morphologies of QDs (especially compounds containing gallium or arsenic) gradually deviate from ideal hemispheres due to the higher diffusion barriers. Scale bars, 1 μm (**a**(1)–**e**(1)), 200 nm (**a**(2)–**e**(4)).

between them, analogous to the vdW epitaxial growth of 2D layered materials[24–26]. As shown in Fig. 2d,e, the pseudohexagonally symmetric (111) facet of InSb, with its <110> direction aligned along the <11$\bar{2}$0> direction in the MoS_2 (0001) plane, was the most energetically favourable state compared with other low-index facets, such as (100) and (110). This InSb–(111)/MoS_2–(0001) configuration was consistent with the observed lattice arrangement in Fig. 1g.

Wafer-scale production of InAs QDs on fluorophlogopite mica

Constrained by the mechanical exfoliation technique, the size of vdW surfaces is typically limited to several tens of micrometres, which is not suitable for the large-scale production and integrated application of QDs. To extend the vdW epitaxial growth of QDs to an integration level, a freshly cleaved 2 inch vdW surface of fluorophlogopite mica (FL mica) was used as the substrate for the fabrication of InAs QDs (Fig. 3a). Both the size and density of the InAs QDs were uniform across the entire wafer (Extended Data Fig. 2), benefiting from substrate rotation and the uniform temperature distribution. Specifically, the average size of the QDs could be manipulated from ~10 nm to ~50 nm simply by increasing the growth time from 30 s to 5 min (Extended Data Fig. 3). The density of the InAs QDs strongly depended on temperature (Fig. 3b), as a small temperature variation (from 200 °C to 340 °C) could result in a large range of densities (from 1.6×10^{11} cm^{-2} to 2.5×10^{7} cm^{-2}). This characteristic offers an important advantage in designing device functionalities, ranging from laser emitters to single-photon sources[27–29].

In situ characterization via reflective high-energy electron diffraction was used to investigate the vdW epitaxial relationship between InAs QDs and FL mica. As shown in Fig. 3c, interface symmetry was also achieved: the line connecting the (111) and (000) facets of InAs QDs was parallel to the diffraction lines of FL mica. This observation suggested that the (111) facet of InAs QDs was in contact with the vdW surface of FL mica (Extended Data Fig. 4). Moreover, the diffraction spots of InAs QDs were not situated on the diffraction lines of FL mica, verifying their non-coherent vdW epitaxial growth. Notably, there were two sets of diffraction spots for the InAs QDs (denoted by red and yellow arrows, respectively), implying two equal-probability orientations of InAs QDs due to their degenerate energies on the pseudohexagonal lattice surface of FL mica (Supplementary Fig. 4). The representative photoluminescence (PL) spectrum of our as-grown InAs QDs (diameter, ~35 nm) contained a characteristic peak located at 1.93 μm (Fig. 3d). A blueshift was observed as the QD size decreased (Supplementary Fig. 5). The Raman spectra of the InAs QDs on FL mica showed characteristic peaks located at 212 and 230 cm^{-1}, which were both redshifted compared with those of their bulk counterparts, confirming the synergetic effect of their stress-free nature and size reduction[23,30] (Fig. 3e).

Although vdW surfaces without dangling bonds do not introduce strain on epitaxial QDs as covalent bonds do, the strength of vdW

https://doi.org/10.1038/s44160-024-00562-0

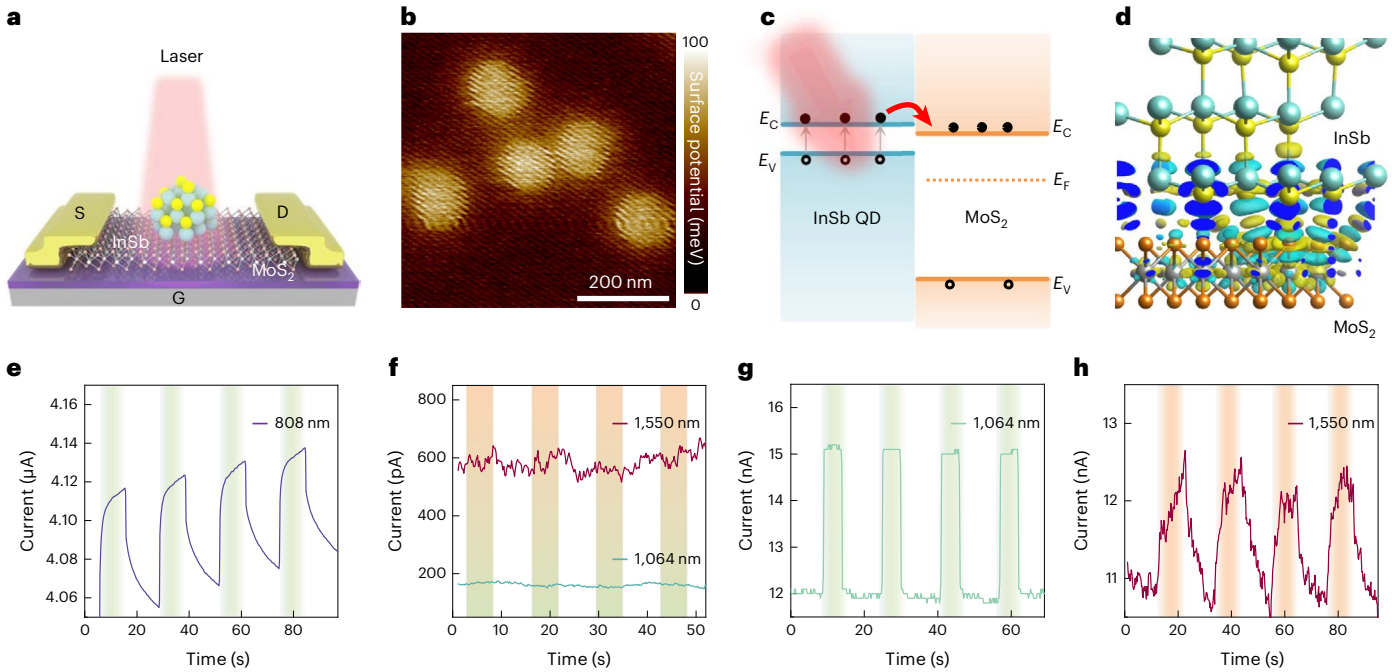

Fig. 5 | Photodetection of the InSb QDs/MoS_2 heterostructure. a, Schematic of the InSb QDs/MoS_2 photodetector. The current was measured by applying a bias to the source (S) and drain (D) electrodes with the regulation of the gate (G) electrode. **b**, The surface potential difference indicates a tiny gap of ~0.1 eV between the conduction band minima of InSb QDs and MoS_2. **c**, Charge transfer driven by an intrinsic electric field with type II band alignment, showing electron flow from InSb QDs to MoS_2 under infrared photoexcitation. E_C, E_V and E_F indicate the conduction band minimum, the valance band maximum and the Fermi level, respectively. **d**, Differential charge density diagram simulated by theoretical calculations, predicting electron flow from the InSb surface to the MoS_2 surface. **e**, Enhanced photocurrent of InSb QDs/MoS_2 at 808 nm, which was in the response range of both InSb and MoS_2. The slow decay of the photocurrent arises from the intrinsic properties of MoS_2. **f**, No photoresponse was observed at wavelengths of 1,064 nm and 1,550 nm for individual MoS_2 flakes. **g**,**h**, Photoresponses of the InSb QDs/MoS_2 heterostructure at 1,064 nm (**g**) and 1,550 nm (**h**). The vertical shaded bands corresponding to the photocurrents indicate periodic illuminations. The slow decay of the photocurrent at 1,550 nm was attributed to thermal noise.

interactions plays a considerable role in the regulation of QDs. Here, graphene, MoS_2 and hexagonal boron nitride (hBN) were simulated as vdW surfaces for InAs QD growth due to their hexagonal symmetry but distinct surface properties (Fig. 3f). Specifically, the zero-bandgap and out-of-plane delocalized π electrons of graphene led to the strongest binding to QDs, whereas the binding between the QDs and MoS_2 or hBN was weaker due to their relatively inert surfaces. Thus, the electronic structure of 2D layered substrates provided a novel degree of freedom for modulating the coupling strength and thus the morphology of QDs.

Universal synthesis of QDs by vdW epitaxy

Our vdW epitaxy strategy for QDs has been demonstrated to be applicable to the synthesis of various high-quality QDs. As shown in Fig. 4, five types of QDs (namely, the III–V compounds InAs, GaAs, InSb and GaSb and the IV–VI compound SnTe) were successfully grown on four distinct vdW substrates (hBN, FL mica, MoS_2 and graphene). The morphologies of the same QD species varied due to the differing interfacial coupling strengths between the QDs and vdW surfaces, which determined the atom migration efficiency on the surfaces, as shown in Fig. 3f. Specifically, anomalous morphologies such as flakes or rods were more frequently observed on graphene surfaces due to their strong binding with QDs, while well-shaped hemispheres were usually accessible on the inert surfaces of hBN and FL mica. Additionally, the intrinsic atom dispersion characteristics affected the QD morphology. For instance, QDs containing arsenic often deviate from a hemisphere structure, which can be attributed to the tendency of arsenic atoms to form multiatomic clusters (mainly As_4)[31]. These arsenic clusters are difficult to separate into monomers, resulting in insufficient and unbalanced collision and chemical bond formation, ultimately leading to irregularly shaped QDs (Fig. 4a(3),(4),b(3),(4)). However, notably, an ideal stoichiometric ratio of ~1 in arsenic-containing III–V QDs was well preserved even at low growth temperatures because excess arsenic atoms easily desorbed from vdW surfaces (Supplementary Fig. 6 and Supplementary Note 1). On the other hand, SnTe with a NaCl crystal structure exhibited ideal appearances on all four vdW surfaces, benefiting from the monodispersion of its component atoms and the relatively fast migration of atoms on the vdW surfaces.

This epitaxy strategy for vdW surfaces offers notable advantages for the fabrication of stress-free III–V QDs, such as InSb, GaAs and GaSb, which are difficult to prepare through the SK mode. Moreover, a large growth window (substrate temperature, 120–350 °C; beam flux intensity, ~2 orders of magnitude variation) was permissible, allowing the universal synthesis of a wide variety of QD species under extreme growth conditions. More intriguingly, by prepatterning vdW substrates, regularly distributed 0D/2D arrays were successfully fabricated by the selective growth of QDs, which is an impressive route toward QD scalability (Supplementary Fig. 7).

Photoresponse of the InSb QDs/MoS_2 heterostructure

The exceptional photon absorption characteristics of QDs, which are not constrained by selection rules, unlike those of quantum well photodetectors, play a crucial role in enhancing the response of photodetectors based on 2D vdW semiconductors[32–34]. Kelvin potential force microscopy was used to measure the difference in surface potential between InSb QDs and the MoS_2 layer, revealing a tiny gap of ~0.1 eV between the conduction band minimum and thus a type II band alignment in the heterostructure (Fig. 5b). Upon infrared photoexcitation, photon-induced electrons in InSb QDs were assumed to drift toward the MoS_2 layer, driven by the built-in electrical field (Fig. 5c). This process was used to monitor the photocurrent through electrodes deposited on MoS_2, as illustrated in Fig. 5a. As shown in the differential charge

density diagram (Fig. 5d), the regions of electron loss (blue clouds) and electron reception (yellow clouds) were predominantly located on the InSb QD subface and MoS_2 surface, respectively, validating the tendency for effective charge transfer from InSb to MoS_2. This phenomenon contributed to an enhanced photocurrent for InSb QDs/MoS_2 heterostructure in comparison to that for individual MoS_2 flakes upon excitation at a wavelength of 808 nm (within the response range of both InSb QDs and MoS_2) (Supplementary Fig. 8). More importantly, a pronounced photoresponse was stimulated in the mixed-dimensional heterostructures, even at certain infrared wavelengths unavailable for individual MoS_2 flakes (1,064 nm and 1,550 nm, as shown in Fig. 5e–h), remarkably extending the response capabilities of 2D MoS_2 photodetectors. It was suggested that the intrinsic coupling between QDs and 2D layered materials facilitated the construction of additional charge-transfer channels, thereby enhancing device performance and broadening the functional scope of the material.

Conclusion

This study demonstrated that highly controllable growth of QDs with broadened components can be achieved by using the vdW surfaces of 2D layered materials as substrates. Based on the moderate and adjustable coupling between the QD and substrate, this method enabled the QDs to be free from the restriction of coherent epitaxy, the influence of stress, and external chemical pollution. Moreover, complementary techniques, such as optimization of the III–V QD morphology and construction of multilayer heterostructures, also need to be developed. In theory, non-layered stable phases can be grown into QDs on any vdW surface. The combination of QDs and 2D layered materials resulted in the formation of intrinsic vdW interfaces and generated effective charge-transfer channels, providing a new platform for investigating mixed-dimensional heterostructures and widening the potential applications of low-dimensional quantum systems.

Methods

Synthesis recipe

hBN, MoS_2 and graphene flakes, with thicknesses from several to tens of nanometres, were mechanically exfoliated from their bulk crystals (Onway-Technology), and then transferred onto 2 × 2 cm^2 SiO_2/Si substrates. Subsequently, the prepared substrate of SiO_2/Si or the 2 inch FL mica wafer was mounted on a molybdenum holder and placed in the MBE buffer chamber. The holder was heated to 150–350 °C to eliminate adsorbed water and gas impurities. The holder was then maintained at 120–220 °C in the growth chamber to allow the growth of QDs of different epitaxies. Finally, the substrate was naturally cooled down to room temperature, without the need for group V flux protection.

InAs QDs on hBN. The beam equivalent pressure of indium and arsenic was maintained at 5×10^{-8} torr and 1.5×10^{-6} torr, respectively. The growth temperature was kept at 200 °C for 1.5 min.

GaAs QDs on hBN. The beam equivalent pressure of gallium and arsenic was maintained at 3×10^{-8} torr and 1.5×10^{-6} torr, respectively. The growth temperature was kept at 200 °C for 2 min.

InSb QDs on hBN. The beam equivalent pressure of indium and antimony was maintained at 5×10^{-8} torr and 3×10^{-7} torr, respectively. The growth temperature was kept at 180 °C for 2 min.

GaSb QDs on hBN. The beam equivalent pressure of gallium and antimony was maintained at 3×10^{-8} torr and 3×10^{-7} torr, respectively. The growth temperature was kept at 200 °C for 2 min.

SnTe QDs on hBN. The beam equivalent pressure of tin and tellurium was maintained at 1×10^{-8} torr and 8×10^{-7} torr, respectively. The growth temperature was kept at 180 °C for 1 min.

InAs QDs on FL mica. The beam equivalent pressure of indium and arsenic was maintained at 5×10^{-8} torr and 1.5×10^{-6} torr, respectively. The growth temperature was kept at 210 °C for 7 min.

GaAs QDs on FL mica. The beam equivalent pressure of gallium and arsenic was maintained at 3×10^{-8} torr and 1.5×10^{-6} torr, respectively. The growth temperature was kept at 210 °C for 6.5 min.

InSb QDs on FL mica. The beam equivalent pressure of indium and antimony was maintained at 5×10^{-8} torr and 3×10^{-7} torr, respectively. The growth temperature was kept at 220 °C for 6 min.

GaSb QDs on FL mica. The beam equivalent pressure of gallium and antimony was maintained at 3×10^{-8} torr and 3×10^{-7} torr, respectively. The growth temperature was kept at 210 °C for 6.5 min.

SnTe QDs on FL mica. The beam equivalent pressure of tin and tellurium was maintained at 1×10^{-8} torr and 8×10^{-7} torr, respectively. The growth temperature was kept at 200 °C for 5 min.

InAs QDs on MoS_2. The beam equivalent pressure of indium and arsenic was maintained at 5×10^{-8} torr and 1.5×10^{-6} torr, respectively. The growth temperature was kept at 160 °C for 1 min.

GaAs QDs on MoS_2. The beam equivalent pressure of gallium and arsenic was maintained at 3×10^{-8} torr and 1.5×10^{-6} torr, respectively. The growth temperature was kept at 150 °C for 1.5 min.

InSb QDs on MoS_2. The beam equivalent pressure of indium and antimony was maintained at 5×10^{-8} torr and 3×10^{-7} torr, respectively. The growth temperature was kept at 150 °C for 1 min.

GaSb QDs on MoS_2. The beam equivalent pressure of gallium and antimony was maintained at 3×10^{-8} torr and 3×10^{-7} torr, respectively. The growth temperature was kept at 150 °C for 1.5 min.

SnTe QDs on MoS_2. The beam equivalent pressure of tin and tellurium was maintained at 1×10^{-8} torr and 8×10^{-7} torr, respectively. The growth temperature was kept at 160 °C for 5 min.

InAs QDs on graphene. The beam equivalent pressure of indium and arsenic was maintained at 5×10^{-8} torr and 1.5×10^{-6} torr, respectively. The growth temperature was kept at 220 °C for 40 s.

GaAs QDs on graphene. The beam equivalent pressure of gallium and arsenic was maintained at 3×10^{-8} torr and 1.5×10^{-6} torr, respectively. The growth temperature was kept at 180 °C for 1 min.

InSb QDs on graphene. The beam equivalent pressure of indium and antimony was maintained at 5×10^{-8} torr and 3×10^{-7} torr, respectively. The growth temperature was kept at 160 °C for 1 min.

GaSb QDs on graphene. The beam equivalent pressure of gallium and antimony was maintained at 3×10^{-8} torr and 3×10^{-7} torr, respectively. The growth temperature was kept at 160 °C for 1 min.

SnTe QDs on graphene. The beam equivalent pressure of tin and tellurium was maintained at 1×10^{-8} torr and 8×10^{-7} torr, respectively. The growth temperature was kept at 150 °C for 3 min.

Sample characterization

The morphologies of the QDs were determined by atomic force microscopy (Nano scope IIIa, Bruker and MFP-3D Origin, Oxford). Optical images of QDs on vdW surfaces were taken by dark-field microscopy (BX53M, Olympus). For characterization by high-resolution TEM and

EDS, InSb QDs/MoS_2 and InAs QDs/FL mica were cut with a focused ion beam then analysed by TEM (FEI Talos F200X). High-resolution electronic images of QDs on hBN were obtained by scanning electron microsopy (Hitachi s4800). The Raman spectra were measured with a microscopic confocal laser Raman spectrometer (InVia, Renishaw) with a 532 nm laser. The PL spectrum of InAs QDs/FL mica was obtained with an infrared PL spectrometer (80V, Bruker) at 77 K. The PL spectra of InAs QDs/hBN and GaAs QDs/hBN were measured at room temperature in a nitrogen-filled glovebox (Supplementary Fig. 9) using a PL spectrometer (WITec alpha 300R system).

Fabrication and measurement of the InSb QD/MoS_2 device

Photolithography was used to produce gold ribbons 100 nm thick. After MoS_2 had been mechanically exfoliated and transferred to SiO_2/Si substrate using polydimethylsiloxane adhesive film, gold ribbons were dry transferred on to the sides of MoS_2 flakes to serve as the source/drain electrodes. Then, the substrate was placed in the MBE system; after degassing the system, InSb QDs were grown. The active area was illuminated and the photocurrent was collected with a semiconductor analyser (Agilent Technologies B1500A). The optical power (P) and spot area (A) for different laser wavelengths were as follows: for 638 nm, $P = 20$ mW, $A = 0.292$ cm^2; for 808 nm, $P = 104$ mW, $A = 0.503$ cm^2; for 1,064 nm, $P = 228$ mW, $A = 1.131$ cm^2; for 1,550 nm, $P = 150$ mW, $A = 0.502$ cm^2. The source/drain voltage was fixed at 1.5 V.

DFT calculations

Our calculations were carried out using the projector augmented wave as implemented in the Vienna Ab initio Simulation Package[35,36]. The Perdew–Burke–Ernzerhof approximation[37] was used for the exchange-correlation functional. The cut-off energy of the plane-wave basis was set to 400 eV and self-consistent calculations did not stop until energy changes were $<1 \times 10^{-6}$ eV. The minimum-energy pathway and diffusion barriers for indium and antimony atoms on MoS_2 and the InSb–Sb(111) surface were obtained from the climbing-image nudged elastic band method as implemented within the Vienna Ab initio Simulation Package[38,39]. All structures were fully relaxed until the Hellmann–Feynman force on each atom reached <0.05 eV Å^{-1}.

Data availability

All of the source data supporting the findings of this study are available in the main text, Extended Data and Supplementary Information.

References

1. Hong, H. et al. Giant enhancement of optical nonlinearity in two-dimensional materials by multiphoton-excitation resonance energy transfer from quantum dots. *Nat. Photon.* **15**, 510–515 (2021).
2. Wang, Y. et al. Near resonant and nonresonant third-order optical nonlinearities of colloidal InP/ZnS quantum dots. *Appl. Phys. Lett.* **102**, 021917 (2013).
3. Chen, S. et al. Electrically pumped continuous-wave III–V quantum dot lasers on silicon. *Nat. Photon.* **10**, 307–311 (2016).
4. Park, Y.-S. et al. Colloidal quantum dot lasers. *Nat. Rev. Mater.* **6**, 382–401 (2021).
5. Whitworth, G., Dalmases, M., Taghipour, N. & Konstantatos, G. Solution-processed PbS quantum dot infrared laser with room-temperature tunable emission in the optical telecommunications window. *Nat. Photon.* **15**, 738–742 (2021).
6. Keuleyan, S., Lhuillier, E., Brajuskovic, V. & Guyot-Sionnest, P. Mid-infrared HgTe colloidal quantum dot photodetectors. *Nat. Photon.* **5**, 489–493 (2011).
7. Konstantatos, G. et al. Ultrasensitive solution-cast quantum dot photodetectors. *Nature* **442**, 180–183 (2006).
8. García de Arquer, F. P., Armin, A., Meredith, P. & Sargent, E. H. Solution-processed semiconductors for next-generation photodetectors. *Nat. Rev. Mater.* **2**, 1–17 (2017).
9. Lu, C.-Y. & Pan, J.-W. Quantum-dot single-photon sources for the quantum internet. *Nat. Nanotech.* **16**, 1294–1296 (2021).
10. Kandel, Y. P. et al. Adiabatic quantum state transfer in a semiconductor quantum-dot spin chain. *Nat. Commun.* **12**, 2156 (2021).
11. Kagan, C. R., Lifshitz, E., Sargent, E. H. & Talapin, D. V. Building devices from colloidal quantum dots. *Science* **353**, aac5523 (2016).
12. Liu, M. et al. Colloidal quantum dot electronics. *Nat. Electron.* **4**, 548–558 (2021).
13. Liu, S. et al. Efficiently passivated PbSe quantum dot solids for infrared photovoltaics. *ACS Nano* **15**, 3376–3386 (2021).
14. Böhm, M. L. et al. Lead telluride quantum dot solar cells displaying external quantum efficiencies exceeding 120%. *Nano Lett.* **15**, 7987–7993 (2015).
15. Won, Y.-H. et al. Highly efficient and stable InP/ZnSe/ZnS quantum dot light-emitting diodes. *Nature* **575**, 634–638 (2019).
16. Lim, J., Park, Y.-S. & Klimov, V. I. Optical gain in colloidal quantum dots achieved with direct-current electrical pumping. *Nat. Mater.* **17**, 42–49 (2018).
17. Livache, C. et al. A colloidal quantum dot infrared photodetector and its use for intraband detection. *Nat. Commun.* **10**, 2125 (2019).
18. Chen, B. et al. Low dark current high gain InAs quantum dot avalanche photodiodes monolithically grown on Si. *ACS Photon.* **7**, 528–533 (2020).
19. Liu, H. et al. Long-wavelength InAs/GaAs quantum-dot laser diode monolithically grown on Ge substrate. *Nat. Photon.* **5**, 416–419 (2011).
20. Huang, J. et al. Defect characterization of InAs/InGaAs quantum dot p-i-n photodetector grown on GaAs-on-V-grooved-Si substrate. *ACS Photon.* **6**, 1100–1105 (2019).
21. Holewa, P. et al. Thermal stability of emission from single InGaAs/GaAs quantum dots at the telecom O-band. *Sci. Rep.* **10**, 21816 (2020).
22. Prieto, J., Armelles, G., Groenen, J. & Carles, R. Size and strain effects in the E^1-like optical transitions of InAs/InP self-assembled quantum dot structures. *Appl. Phys. Lett.* **74**, 99–101 (1999).
23. Guanjie, Z. et al. Raman scattering of InAs quantum dots with different deposition thicknesses. *J. Semicond.* **27**, 1012–1015 (2006).
24. Dong, J., Zhang, L., Dai, X. & Ding, F. The epitaxy of 2D materials growth. *Nat. Commun.* **11**, 5862 (2020).
25. Zhang, L., Dong, J. & Ding, F. Strategies, status, and challenges in wafer scale single crystalline two-dimensional materials synthesis. *Chem. Rev.* **121**, 6321–6372 (2021).
26. Liu, C., Wang, L., Qi, J. & Liu, K. Designed growth of large-size 2D single crystals. *Adv. Mater.* **32**, 2000046 (2020).
27. Chang, W.-H. et al. Efficient single-photon sources based on low-density quantum dots in photonic-crystal nanocavities. *Phys. Rev. Lett.* **96**, 117401 (2006).
28. Yuan, Z. et al. Electrically driven single-photon source. *Science* **295**, 102–105 (2002).
29. Uppu, R. et al. On-chip deterministic operation of quantum dots in dual-mode waveguides for a plug-and-play single-photon source. *Nat. Commun.* **11**, 3782 (2020).
30. Ibanez, J. et al. Strain relaxation in stacked InAs/GaAs quantum dots studied by Raman scattering. *Appl. Phys. Lett.* **83**, 3069–3071 (2003).
31. Künzel, H. & Ploog, K. The effect of As_2 and As_4 molecular beam species on photoluminescence of molecular beam epitaxially grown GaAs. *Appl. Phys. Lett.* **37**, 416–418 (1980).
32. Ma, H. et al. Enhanced hot carrier up-conversion in graphene by quantum dot coating. *Adv. Opt. Mater.* **10**, 2101563 (2022).

33. Hu, C. et al. Synergistic effect of hybrid PbS quantum dots/2D-WSe_2 toward high performance and broadband phototransistors. *Adv. Funct. Mater.* **27**, 1603605 (2017).
34. Konstantatos, G. et al. Hybrid graphene–quantum dot phototransistors with ultrahigh gain. *Nat. Nanotech.* **7**, 363–368 (2012).
35. Kresse, G. & Furthmüller, J. Efficiency of ab-initio total energy calculations for metals and semiconductors using a plane-wave basis set. *Comput. Mater. Sci.* **6**, 15–50 (1996).
36. Kresse, G. & Furthmüller, J. Efficient iterative schemes for ab initio total-energy calculations using a plane-wave basis set. *Phys. Rev. B* **54**, 11169 (1996).
37. Perdew, J. P., Burke, K. & Ernzerhof, M. Generalized gradient approximation made simple. *Phys. Rev. Lett.* **77**, 3865 (1996).
38. Henkelman, G., Uberuaga, B. P. & Jónsson, H. A climbing image nudged elastic band method for finding saddle points and minimum energy paths. *J. Chem. Phys.* **113**, 9901–9904 (2000).
39. Sheppard, D., Terrell, R. & Henkelman, G. Optimization methods for finding minimum energy paths. *J. Chem. Phys.* **128**, 134106 (2008).

Acknowledgements

This work was financially supported by the National Natural Science Foundation of China (grant numbers 62222408 (to S.Z.), 62125404 (to Z.W.), 12274404 (to S.Z.), 62375256 (to J.Y.), 52322205 (to C.L.), 52250398 (to C.L.) and 12274456 (to C.L.)), in part by the Youth Innovation Promotion Association of the Chinese Academy of Sciences (grant number 2022112 (to S.Z.)), the Beijing Natural Science Foundation (grant number Z220005 (to Z.W.)), the National Key Research and Development Program of China (grant numbers 2020YFB1506400 (to Z.W.) and 2022YFA1405600 (to C.L.)), the Strategic Priority Research Program of Chinese Academy of Sciences (grant number XDB43000000 (to Z.W.) and XDB0460000 (to H.-X.D.)), and the CAS Project for Young Scientists in Basic Research (grant number YSBR-026 (to Z.W.)).

Author contributions

S.Z., Z.W., F.L. and C.L. supervised the project. K.X., L.L. and Z.Z. conducted the sample growth and characterizations. K.X. and Z.Z. wrote the article. C.Z. performed the theoretical calculations. J.Y., H.-X.D., J.Z., J.L. and K.L. revised the manuscript. All the authors discussed the results and commented on the manuscript.

Competing interests

The authors declare no competing interests.

Additional information

Extended data is available for this paper at https://doi.org/10.1038/s44160-024-00562-0.

Supplementary information The online version contains supplementary material available at https://doi.org/10.1038/s44160-024-00562-0.

Correspondence and requests for materials should be addressed to Can Liu, Fengqi Liu, Zhongming Wei or Shenqiang Zhai.

Peer review information *Nature Synthesis* thanks Chen Shang and the other, anonymous, reviewer(s) for their contribution to the peer review of this work. Primary Handling Editor: Alexandra Groves, in collaboration with the *Nature Synthesis* team.

https://doi.org/10.1038/s44160-024-00562-0

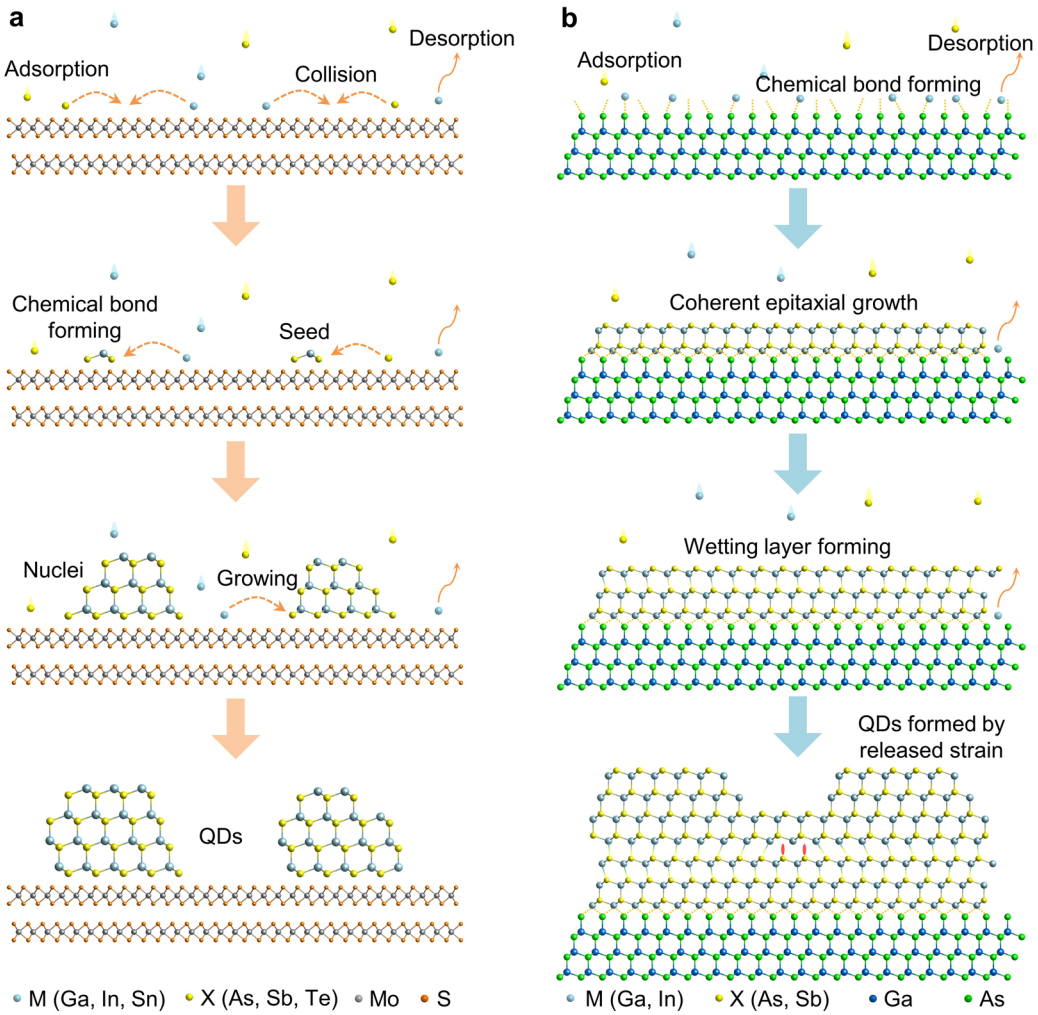

Extended Data Fig. 1 | Schematics of QDs grown by vdW epitaxy and coherent epitaxy. a, The non-layered stable phase tends to reduce the surface energy, hence forming QDs with large aspect ratios on vdW substrates. **b**, Typical coherent epitaxy commonly requires a wetting layer to accumulate stress followed by strain release to form QDs.

https://doi.org/10.1038/s44160-024-00562-0

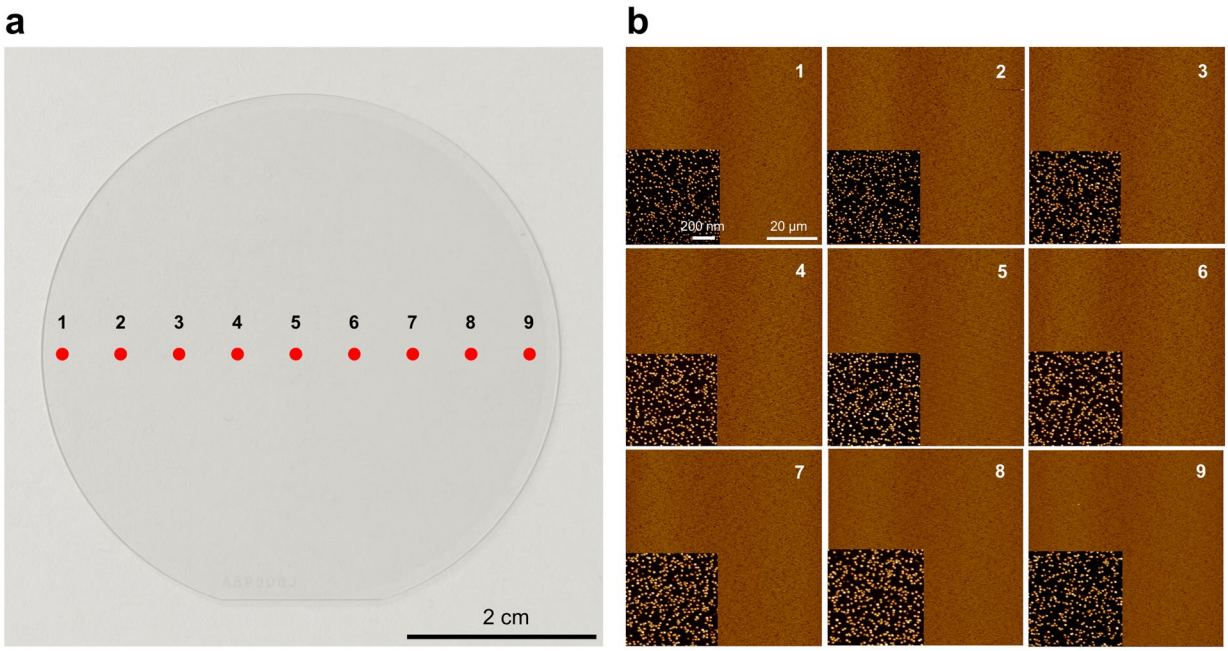

Extended Data Fig. 2 | InAs QDs grown on wafer-scale FL mica with highly uniform distribution of size and density. a, Photograph of a 2-inch FL mica on which InAs QDs were grown. **b**, AFM images of InAs QDs grown on the 2-inch FL mica wafer at nine positions denoted by the red dots. The insets show the magnified views of InAs QDs at the centre square with 200 nm sides of each position (80 μm×80 μm).

https://doi.org/10.1038/s44160-024-00562-0

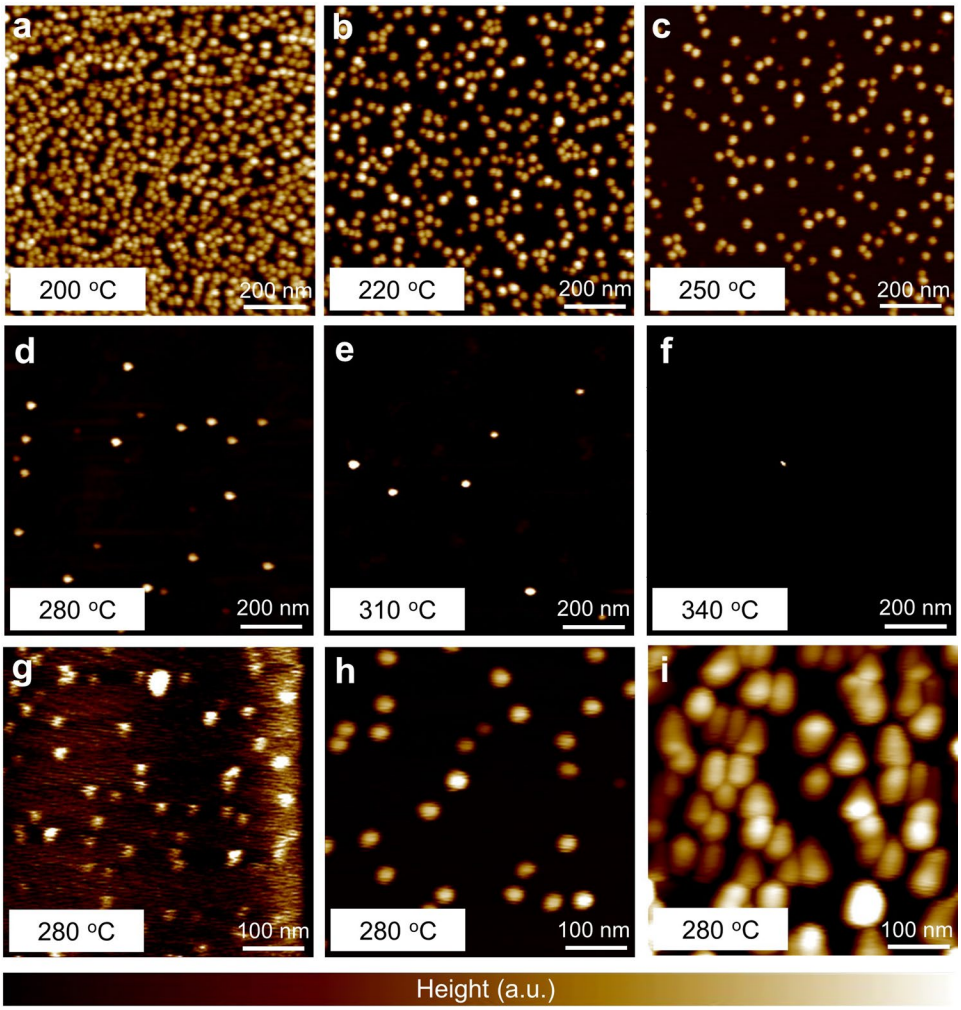

Extended Data Fig. 3 | Regulation of the QD size and density by substrate temperature and growth time. a-f, InAs QDs grown on FL mica at 200 °C, 220 °C, 250 °C, 280 °C, 310 °C, and 340 °C for 1 min, leading to densities of 1.6×10^{11} cm^{-2}, 2.5×10^{10} cm^{-2}, 1.0×10^{9} cm^{-2}, 2.4×10^{8} cm^{-2}, 4.0×10^{7} cm^{-2}, and 2.5×10^{7} cm^{-2}, respectively. **g-i**, InAs QDs grown on FL mica at 280 °C for 30 s, 3 min, and 5 min, leading to average sizes of 10 nm, 20 nm, and 50 nm, respectively.

https://doi.org/10.1038/s44160-024-00562-0

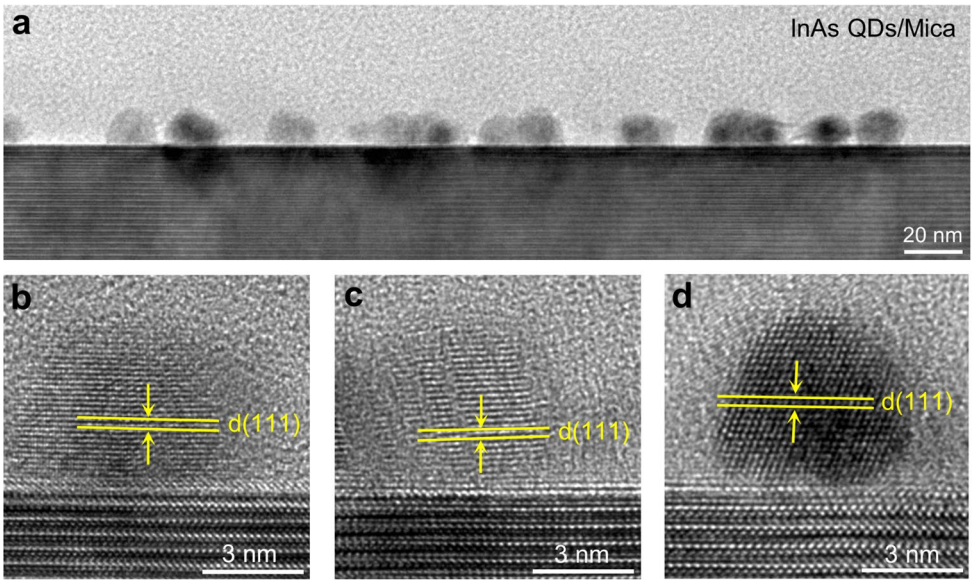

Extended Data Fig. 4 | Epitaxial relationship between InAs QDs and FL mica. a, Cross-sectional high-resolution transmission electron microscopy (HRTEM) image of a series of InAs QDs on FL mica. **b-d**, Three magnified views of InAs QDs with lattice configuration of InAs-(111) contacting the vdW surface of FL mica.

https://doi.org/10.1038/s44160-024-00562-0

Extended Data Table 1 | Thickness-dependent density and size of InSb QDs on MoS_2

MoS_2 thickness	QD density	QD size	Typical AFM image
0.7 nm (1 layer) Monolayer	~3.2×10^{10} cm^{-2}	~30 nm	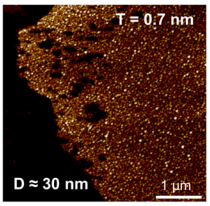
3 nm (4 layers) Few layers	~9.5×10^{9} cm^{-2}	~70 nm	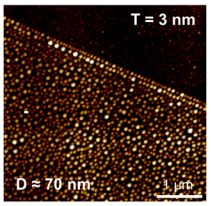
30 nm (42 layers) Bulk	~4.0×10^{9} cm^{-2}	~100 nm	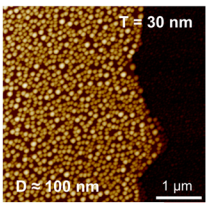

T: Thickness of MoS_2; D: Average diameter of InSb QDs